All-Optical Entanglement Swapping

Shengshuai Liu,[1] Yanbo Lou,[1] Yingxuan Chen,[1] and Jietai Jing[1,2,3,4,*]
[1]State Key Laboratory of Precision Spectroscopy, Joint Institute of Advanced Science and Technology, School of Physics and Electronic Science, East China Normal University, Shanghai 200062, China
[2]CAS Center for Excellence in Ultra-intense Laser Science, Shanghai 201800, China
[3]Department of Physics, Zhejiang University, Hangzhou 310027, China
[4]Collaborative Innovation Center of Extreme Optics, Shanxi University, Taiyuan, Shanxi 030006, China

(Received 4 September 2021; revised 22 December 2021; accepted 2 February 2022; published 11 February 2022)

Entanglement swapping, which is a core component of quantum network and an important platform for testing the foundation of quantum mechanics, can enable the entangling of two independent particles without direct interaction both in discrete variable and continuous variable systems. Conventionally, the realization of entanglement swapping relies on the Bell-state measurement. In particular, for entanglement swapping in continuous variable regime, such Bell-state measurement involves the optic-electro and electro-optic conversion, which limits the applications of the entanglement swapping for constructing broadband quantum network. In this Letter, we propose and demonstrate a measurement-free all-optical entanglement swapping. In our scheme, a high-gain parametric amplifier based on the four-wave mixing process is exploited to realize the function of Bell-state measurement without detection, which avoids the introduction of the optic-electro and electro-optic conversion. Our results provide an all-optical paradigm for implementing entanglement swapping and pave the way to construct a measurement-free all-optical broadband quantum network.

DOI: 10.1103/PhysRevLett.128.060503

Entanglement swapping is at the heart of a future quantum network since it is an indispensable part of a quantum repeater [1]. In such protocol, through the Bell-state measurement (BSM) of two particles from two independent entanglement sources, the remaining particles, which have never been directly interacted, can be entangled. Since first proposed in 1993 [2], it has been extensively studied in both discrete variable (DV) and continuous variable (CV) systems [3,4]. In the DV regime, entanglement swapping has been experimentally implemented with various entanglement sources, including polarization [5–7], energy-time [8], orbital angular momentum [9], and superconducting qubit [10] entanglement. Such a striking concept of entanglement swapping has also been transplanted to the CV regime of quantum information, aiming at demonstrating its unconditional implementation [11–13]. Its realization is based on the quadrature entanglement of optical fields from parametric down-conversion and feed-forward techniques [14,15]. However, such feed-forward technique involves the optic-electro and electro-optic conversion, which limits the bandwidth of entanglement swapping. In this sense, the all-optical version of entanglement swapping is needed to avoid optic-electro and electro-optic conversion, which remains unexplored both theoretically and experimentally.

Recently, we have experimentally demonstrated an all-optical multichannel quantum teleportation protocol [16,17]. Such an all-optical scheme is measurement free, thus avoiding the optic-electro and electro-optic conversions in the usual quantum information protocol [18]. Therefore, based on such an all-optical scheme, it is prospective to develop an all-optical version of entanglement swapping. In this Letter, we theoretically propose and experimentally demonstrate a scheme of measurement-free all-optical entanglement swapping (AOES), in which a low-noise parametric amplifier (PA) based on a double-Λ configuration four-wave mixing (FWM) [17,19–23] is utilized to realize the function of the BSM without detection and a beam splitter is used for state displacement. Two initially separable optical fields become entangled after AOES with quantum correlation degrees of 0.43 ± 0.06 dB and 0.42 ± 0.05 dB below the corresponding shot-noise limit (SNL) for amplitude and phase quadratures, respectively.

Figure 1 shows the detailed experimental setup for AOES. The two Einstein-Podolsky-Rosen (EPR) entangled states [24] used for implementing AOES are generated from the double-Λ configuration FWM process in ^{85}Rb vapor cell. Our optical system is based on a cavity stabilized Ti:sapphire laser whose frequency is about 1.1 GHz blue detuned from the ^{85}Rb D1 line ($5S_{1/2}, F = 2 \rightarrow 5P_{1/2}$). Three polarization beam splitters (PBSs) and three half wave plates (HWPs) are used to divide the laser into four parts. The first part, which is horizontally polarized and has a power of about 200 mW, passes through an acousto-optic modulator (AOM) to generate the input signal beam $\hat{a}_0$ which is redshifted about 3.04 GHz from the pump beam and has a power of about 1 μW. This signal beam with a waist of about 260 μm at the

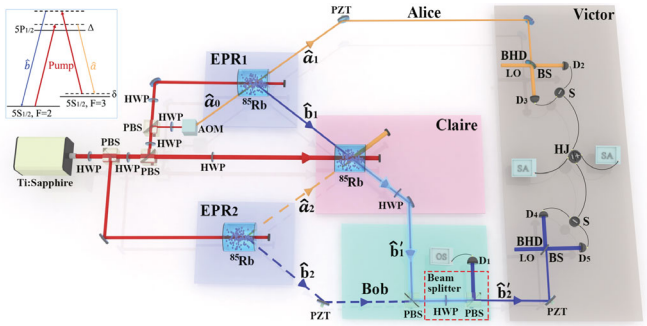

FIG. 1. Detailed experimental setup for AOES. The resolution bandwidth (RBW) of the SA is 1 MHz. The video bandwidth (VBW) of the SA is 100 Hz. Inset, Energy level diagram of FWM process. Δ, one-photon detuning; δ, two-photon detuning.

center of the vapor cell is used for the locking of balanced homodyne detection (BHD) [23]. The second (third) part with a waist of about 530 μm at the center of vapor cell, which is vertically polarized and has a power of about 80 mW, is served as the pump beam of the FWM_1 (FWM_2) in a ^{85}Rb vapor cell for producing EPR_1 (EPR_2). Since the powers of these pump beams are very strong, they can be considered as classical fields under the "undepleted pump" approximation [25]. The two ^{85}Rb vapor cells are 12 mm long and stabilized at 113 °C. As shown in the inset of Fig. 1, in this double-Λ configuration FWM process, two pump photons convert to one photon of signal beam (redshifted from the pump beam) and one photon of idler beam (blueshifted from the pump beam). In this way, the interaction Hamiltonian for these two FWM processes can be described as

$$\begin{aligned}\hat{H}_1 &= i\hbar\gamma_1\hat{a}_1^\dagger\hat{b}_1^\dagger + \mathrm{H.c.},\\ \hat{H}_2 &= i\hbar\gamma_2\hat{a}_2^\dagger\hat{b}_2^\dagger + \mathrm{H.c},\end{aligned} \tag{1}$$

where $\hat{a}_1^\dagger$ ($\hat{a}_2^\dagger$) and $\hat{b}_1^\dagger$ ($\hat{b}_2^\dagger$) are the creation operators associated with signal and idler beams for EPR_1 (EPR_2), respectively. H.c. is the Hermitian conjugate. γ_1 (γ_2) is the interaction strength of FWM process for generating EPR_1 (EPR_2), and the intensity gain is $G_1 = \cosh^2(\gamma_1\tau)$ [$G_2 = \cosh^2(\gamma_2\tau)$] for FWM_1 (FWM_2). τ is the interaction timescale. After generation, $\hat{a}_1$ is distributed to Alice, and $\hat{b}_2$ is distributed to Bob. It means that Alice and Bob initially share two independent particles without entanglement. A piezoelectric transducer (PZT) is placed in the path of $\hat{b}_2$ to change the relative phase θ between $\hat{a}_2$ and $\hat{b}_2$. Then, we distribute $\hat{b}_1$ and $\hat{a}_2$ to Claire. Under this situation, if Claire sends the information of $\hat{b}_1$ and $\hat{a}_2$ to Bob, Bob can establish the entanglement with Alice by two initially independent particles, i.e., realizing AOES. Here, Claire uses a low-noise PA based on FWM [17,19–23] to realize the information transfer without detection. The fourth part of the laser (150 mW) serves as the classical pump beam of this FWM process. Claire crosses the pump beam, $\hat{b}_1$, and $\hat{a}_2$ in the center of the third ^{85}Rb vapor cell to implement FWM process. The angle between $\hat{b}_1$ and $\hat{a}_2$ is about 14 mrad and the pump beam is symmetrically crossed with $\hat{b}_1$ and $\hat{a}_2$ beams in the same plane. We set the intensity gain of PA G_3 at $8 \gg 1$, ensuring that the amplified beam $\hat{b}_1'$ can be considered as a classical field [16]. After this amplification process, the information of $\hat{a}_2$ and $\hat{b}_1$ are transferred into $\hat{b}_1'$ [16,17]. In this way, the PA realizes the function of BSM in the traditional entanglement swapping. Then, Claire sends $\hat{b}_1'$ to Bob through a classical all-optical channel. To transfer the information of $\hat{b}_1'$ to $\hat{b}_2$, first Bob utilizes a PBS to combine $\hat{b}_1'$ and $\hat{b}_2$. In this PBS, the amplified beam $\hat{b}_1'$ (vertically polarized) is totally reflected, while beam $\hat{b}_2$ (horizontally polarized) is totally transmitted. Then Bob uses a HWP to rotate the polarizations of these two perpendicularly polarized beams simultaneously. After that, they pass through a second PBS. In this way, the HWP and the second PBS enclosed by red dashed rectangle together play the role of adjustable beam splitter. The transmission of such beam splitter for $\hat{b}_1'$ and $\hat{b}_2$ can be adjusted continuously by rotating the HWP. For our AOES scheme, Bob adjusts the HWP to make the transmission of the amplified beam $\hat{b}_1'$ to $\varepsilon = 1/G_3$, and the transmission of the beam $\hat{b}_2$ to $1-\varepsilon = 1-1/G_3$. In our experiment, $G_3 = 8$ ($\varepsilon = 1/8$), which can be precisely set by the photodetector (D_1) connecting to an oscilloscope (OS). This beam splitter realizes the function of state displacement. After these operations, $\hat{b}_2$ is translated to $\hat{b}_2'$ which can be expressed as

$$\begin{aligned}\hat{b}_2' &= \hat{b}_1 + \sqrt{\frac{G_3-1}{G_3}}(\hat{a}_2^\dagger - \hat{b}_2 e^{-i\theta})\\ &= \hat{b}_1 + \sqrt{\frac{G_3-1}{G_3}}\Big[\hat{v}_2^\dagger(\sqrt{G_2} - \sqrt{G_2-1}e^{-i\theta})\\ &\quad - \hat{v}_3(\sqrt{G_2}e^{-i\theta} - \sqrt{G_2-1})\Big]\\ &= \sqrt{G_1-1}\hat{a}_0^\dagger + \sqrt{G_1}\hat{v}_1\\ &\quad + \sqrt{\frac{G_3-1}{G_3}}\Big[\hat{v}_2^\dagger(\sqrt{G_2} - \sqrt{G_2-1}e^{-i\theta})\\ &\quad - \hat{v}_3(\sqrt{G_2}e^{-i\theta} - \sqrt{G_2-1})\Big],\end{aligned} \tag{2}$$

where $\hat{v}_1$ is the vacuum state involved in FWM_1. $\hat{v}_2$ and $\hat{v}_3$ are the vacuum states involved in FWM_2. The last term in Eq. (2) vanishes under the conditions of $G_2 \gg 1$ and the relative phase $\theta = 0$, leaving as $\hat{b}_2' \approx \hat{b}_1$. It means that two initially independent particles $\hat{a}_1$ and $\hat{b}_2'$ become entangled after AOES.

To characterize the performance of the AOES, we testify quantum entanglement between the two beams $\hat{a}_1$ and $\hat{b}_2'$ at

Victor station. Specifically, we use inseparability to measure quantum entanglement between $\hat{a}_1$ and $\hat{b}_2'$ [26,27], which can be given as $I_{\hat{a}_1,\hat{b}_2'} = \mathrm{Var}(\hat{X}_{\hat{a}_1} - \hat{X}_{\hat{b}_2'}) + \mathrm{Var}(\hat{Y}_{\hat{a}_1} + \hat{Y}_{\hat{b}_2'})$, where $\hat{X}_{\hat{a}_1} = (\hat{a}_1^\dagger + \hat{a}_1)$ $[\hat{X}_{\hat{b}_2'} = (\hat{b}_2'^\dagger + \hat{b}_2')]$ and $\hat{Y}_{\hat{a}_1} = i(\hat{a}_1^\dagger - \hat{a}_1)$ $[\hat{Y}_{\hat{b}_2'} = i(\hat{b}_2'^\dagger - \hat{b}_2')]$ are the amplitude and phase quadratures of the corresponding fields. If $I_{\hat{a}_1,\hat{b}_2'} < 4$ [26,27], the two optical fields $\hat{a}_1$ and $\hat{b}_2'$ are entangled. It indicates that two independent particles $\hat{a}_1$ and $\hat{b}_2'$ become entangled after AOES. Here, we measure the amplitude and phase quadrature variances of $\hat{a}_1$ and $\hat{b}_2'$ by BHD with spectrum analyzer (SA). A PZT is placed in the path of $\hat{a}_1$ $(\hat{b}_2')$ to change the relative phase between $\hat{a}_1$ $(\hat{b}_2')$ and local oscillator (LO). The balanced detector has a transimpedance gain of 10^5 V A^{-1} and a quantum efficiency of 97%.

Our experimental results of AOES are shown in Fig. 2. The amplitude quadrature difference and phase quadrature sum for the AOES measured by Victor's BHD at 1.4 MHz sideband are shown in Fig. 2(a) (locking the phase of BHD to 0) and Fig. 2(b) (locking the phase of BHD to $\pi/2$), respectively. The variances of amplitude quadrature difference $\hat{X}_{\hat{a}_1} - \hat{X}_{\hat{b}_1}$ $(\hat{X}_{\hat{a}_2} - \hat{X}_{\hat{b}_2})$ and phase quadrature sum $\hat{Y}_{\hat{a}_1} + \hat{Y}_{\hat{b}_1}$ $(\hat{Y}_{\hat{a}_2} + \hat{Y}_{\hat{b}_2})$ of the EPR_1 (EPR_2) are 3.65 ± 0.08 and 3.64 ± 0.10 dB $(3.62 \pm 0.09$ and 3.57 ± 0.07 dB) below the corresponding SNL as shown in Figs. 2(c) and 2(d) [Figs. 2(e) and 2(f)], respectively. These results indicate the presence of the initial EPR entanglement between $\hat{a}_1$ and $\hat{b}_1$ ($\hat{a}_2$ and $\hat{b}_2$). As shown in Figs. 2(a) and 2(b), the black traces, measured by blocking $\hat{a}_1$ and $\hat{b}_2'$, are the quadrature variances of the corresponding SNL. The red traces in Figs. 2(a) and 2(b) are obtained by scanning the relative phase θ between the two modes of EPR_2, i.e., $\hat{a}_2$ and $\hat{b}_2$. The measured quadrature variances of the swapped pair by Victor are shown as the minima of red traces in Fig. 2(a) [amplitude quadrature difference $Var(\hat{X}_{\hat{a}_1} - \hat{X}_{\hat{b}_2'})$] and Fig. 2(b) [phase quadrature sum $\mathrm{Var}(\hat{Y}_{\hat{a}_1} + \hat{Y}_{\hat{b}_2'})$]. This is because only the minima of red trace for the variance of amplitude quadrature difference (phase quadrature sum) indicates that the relative phase between $\hat{a}_2$ and $\hat{b}_2$ corresponds to $\hat{X}_{\hat{a}_2} - \hat{X}_{\hat{b}_2}$ $(\hat{Y}_{\hat{a}_2} + \hat{Y}_{\hat{b}_2})$ (see Sec. A of the Supplemental Material for a detailed explanation [28]). The variances of $\mathrm{Var}(\hat{X}_{\hat{a}_1} - \hat{X}_{\hat{b}_2'})$ and $\mathrm{Var}(\hat{Y}_{\hat{a}_1} + \hat{Y}_{\hat{b}_2'})$ are 0.43 ± 0.06 and 0.42 ± 0.05 dB below the corresponding SNL, respectively. Consequently, the inseparability between $\hat{a}_1$ and $\hat{b}_2'$ can be calculated as $3.63 \pm 0.05 < 4$. This demonstrates the existence of quantum entanglement between $\hat{a}_1$ and $\hat{b}_2'$ [26,27]. In this way, we successfully entangle two independent particles without direct interaction by AOES. For comparison, first we block the EPR_2. The measured quadrature variances are shown as green traces in Figs. 2(a) and 2(b), which are 1.01 ± 0.07 and 1.01 ± 0.08 dB above the corresponding SNL, respectively. In addition, we also test the quantum entanglement between $\hat{a}_1$ and $\hat{b}_2'$ by the positivity under partial transposition (PPT) criterion [27,30–32] in this case. The smallest symplectic eigenvalue of covariance matrices for $\hat{a}_1$ and $\hat{b}_2'$ without the aid of EPR_2 is $1.16 \pm 0.01 > 1$, which means that $\hat{a}_1$ and $\hat{b}_2'$ are not entangled anymore [27,30–32]. Second, we measure the correlation between $\hat{a}_1$ and $\hat{b}_2'$ when $\hat{a}_2$ is blocked. The measured quadrature variances are shown as yellow traces in Figs. 2(a) and 2(b), which are 2.23 ± 0.06 and 2.21 ± 0.07 dB above the corresponding SNL, respectively. Moreover, we measure the smallest symplectic eigenvalue of covariance matrices

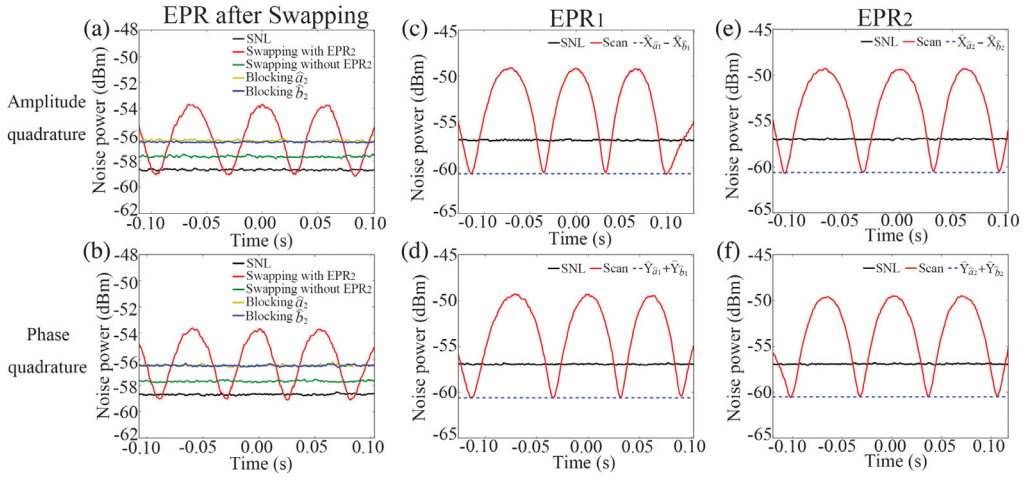

FIG. 2. The results of AOES. (a)[(b)] The variance of amplitude quadrature difference [phase quadrature sum] between $\hat{a}_1$ and $\hat{b}_2'$. (c)[(d)] The amplitude quadrature difference [phase quadrature sum] of EPR_1. The blue dashed line is the variance of amplitude quadrature difference [phase quadrature sum]. The red curve is noise power of the photocurrents output from BHD by scanning the phase of BHD. The black trace represents the corresponding SNL. (e)[(f)] The amplitude quadrature difference [phase quadrature sum] of EPR_2.

for $\hat{a}_1$ and $\hat{b}_2'$ without the aid of $\hat{a}_2$, which is $1.39 \pm 0.01 > 1$. These results clearly show that there is no entanglement between $\hat{a}_1$ and $\hat{b}_2'$ when $\hat{a}_2$ is blocked. In the end, we measure the results when $\hat{b}_2$ is blocked. The measured quadrature variances are shown as blue traces in Figs. 2(a) and 2(b), and the corresponding smallest symplectic eigenvalue of the covariance matrix is $1.38 \pm 0.01 > 1$. These results are similar to the case of blocking $\hat{a}_2$ and clearly show that there is also no entanglement between $\hat{a}_1$ and $\hat{b}_2'$ when $\hat{b}_2$ is blocked. All these results undoubtedly show that EPR entanglement between $\hat{a}_2$ and $\hat{b}_2$ plays an essential role for the implementation of AOES.

To prove that the all-optical channel between Claire and Bob can be considered as a classical channel, we explore how robust this all-optical channel is against loss. When $G_3 = 8$, the experimental inseparabilities of the swapped pair ($\hat{a}_1$ and $\hat{b}_2'$) versus channel loss are shown as red dots in Fig. 3. The theoretically predicted inseparability is represented by the red solid line (see Sec. B of the Supplemental Material for a detailed theoretical derivation [28]). We can see that when the channel loss increases from 0% to 70%, the inseparability value of the swapped pair ($\hat{a}_1$ and $\hat{b}_2'$) only increases from 3.63 to 3.78. It means that the inseparability of the swapped pair is almost immune to the channel loss. In other words, the all-optical channel between Claire and Bob can be considered as a classical channel, and the beam $\hat{b}_1'$ can be considered as a classical optical field. Therefore, $\hat{a}_1$ and $\hat{b}_2'$ have never directly interacted with each other, and our AOES fulfills the requirement of entangling beams that have never directly interacted.

Since our AOES is an all-optical platform, which avoids the optic-electro and electro-optic conversions in standard CV entanglement swapping protocol [14,15], it is worth showing the entanglement sideband that AOES can successfully swap. For this purpose, we increase the analysis frequency from 1.0 to 2.2 MHz with intervals of 0.3 MHz under the same experimental conditions. The corresponding experimental results are shown in Fig. 4. The black straight line represents the upper bound of inseparability. The red dots show the inseparability of $\hat{a}_1$ and $\hat{b}_2'$ versus analysis frequency, which are all below 4. It can be seen that the inseparability induced by AOES slightly decreases when the sideband frequency is above 1.9 MHz. This is because the inseparability of the initial entanglement from FWM process decreases when the sideband frequency is above 1.9 MHz. For comparison, first, by blocking the EPR_2, we also measure the inseparability between $\hat{a}_1$ and $\hat{b}_2'$ shown as green dots in Fig. 4. We can see that the inseparabilities between $\hat{a}_1$ and $\hat{b}_2'$ without the aid of EPR_2 are all above 4. Additionally, we measure the smallest symplectic eigenvalue of covariance matrices for $\hat{a}_1$ and $\hat{b}_2'$ without the aid of EPR_2 from 1.0 to 2.2 MHz, which are all above 1 as shown in Table I. Second, we measure the correlation between $\hat{a}_1$ and $\hat{b}_2'$ for sidebands from 1.0 to 2.2 MHz when $\hat{a}_2$ is blocked, which is shown as yellow dots in Fig. 4. We can see that the inseparabilities between $\hat{a}_1$ and $\hat{b}_2'$ without the aid of $\hat{a}_2$ are all above 4. Moreover, we measure the smallest symplectic eigenvalues of covariance matrices for $\hat{a}_1$ and $\hat{b}_2'$ without the aid of $\hat{a}_2$, which are all above 1 as shown in Table I. These results clearly show that there is no entanglement between $\hat{a}_1$ and $\hat{b}_2'$ when $\hat{a}_2$ is blocked. In the end, we measure the results for sidebands from 1.0 to 2.2 MHz when $\hat{b}_2$ is blocked. The inseparabilities between $\hat{a}_1$ and $\hat{b}_2'$ without the aid of $\hat{b}_2$ are shown as blue dots in Fig. 4, and the corresponding smallest symplectic eigenvalues of covariance matrices are shown in Table I. These results clearly show that there is also no entanglement between $\hat{a}_1$ and $\hat{b}_2'$ when $\hat{b}_2$ is blocked.

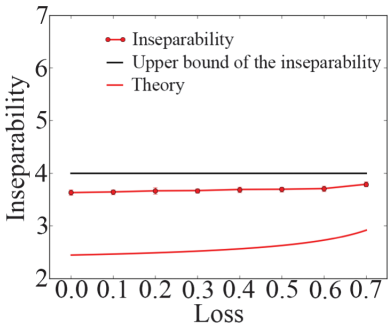

FIG. 3. The inseparability of swapped modes as a function of channel loss. The red dots indicate the inseparability between $\hat{a}_1$ and $\hat{b}_2'$. The black straight line denotes the upper bound of the inseparability. The corresponding theoretically predicted inseparability is represented by the red solid line. The error bars are obtained from the standard deviations of multiple repeated measurements.

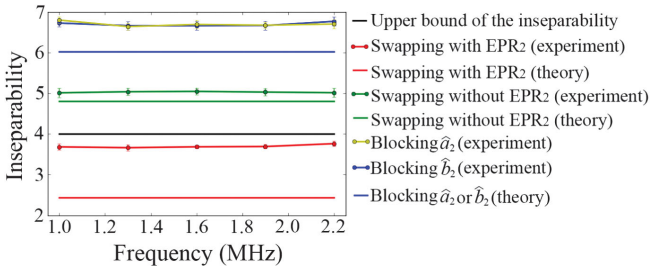

FIG. 4. Inseparabilities versus the sideband frequency. The red dots indicate the inseparability of AOES. The green dots indicate the inseparability between $\hat{a}_1$ and $\hat{b}_2'$ without EPR_2. The yellow (blue) dots indicate the inseparability between $\hat{a}_1$ and $\hat{b}_2'$ without the aid of $\hat{a}_2$ ($\hat{b}_2$). The black straight line denotes the upper bound of the inseparability. The corresponding theoretically predicted inseparabilities are represented by the solid lines with the same colors. The error bars are obtained from the standard deviations of multiple repeated measurements.

TABLE I. Smallest symplectic eigenvalue versus the sideband frequency.

Frequency	1.0 MHz	1.3 MHz	1.6 MHz	1.9 MHz	2.2 MHz
Blocking EPR_2	1.04 ± 0.01	1.13 ± 0.02	1.11 ± 0.01	1.12 ± 0.02	1.08 ± 0.01
Blocking $\hat{a}_2$	1.30 ± 0.01	1.41 ± 0.01	1.38 ± 0.01	1.36 ± 0.01	1.33 ± 0.02
Blocking $\hat{b}_2$	1.31 ± 0.01	1.40 ± 0.02	1.37 ± 0.01	1.34 ± 0.01	1.32 ± 0.02

The corresponding theoretically predicted inseparabilities are represented by the solid lines with the same colors. These results clearly show that we successfully establish the entanglement between $\hat{a}_1$ and $\hat{b}_2'$ from 1.0 to 2.2 MHz by AOES. In our scheme, the AOES bandwidth is mainly limited by the bandwidth of EPR entanglement from FWM process (see Sec. C of the Supplemental Material for a detailed explanation [28]). To improve the bandwidth of AOES, one could use other broadband EPR entanglement to perform AOES. Recently, the THz sideband CV squeezing based on the periodically poled $LiNbO_3$ waveguide has been successfully demonstrated [33], with which the ultra-broadband AOES is promising to be demonstrated in the future.

In addition, the discrepancies between theory and our experimental results in Figs. 3 and 4 are caused by several reasons, such as higher-order irrelevant nonlinear processes, the pump scattering, the detection losses, and the deviation between the inseparability of experimentally generated entanglement and theoretically predicted entanglement (see Sec. D of the Supplemental Material for a detailed explanation [28]).

In summary, we have experimentally demonstrated a scheme of measurement-free AOES. Two initially separable optical fields become entangled after AOES with quantum correlation degrees of 0.43 ± 0.06 and 0.42 ± 0.05 dB below the corresponding SNL for amplitude and phase quadratures, respectively. Moreover, we have shown that AOES can swap the entanglement for the bandwidth ranging from 1.0 to 2.2 MHz. Our AOES scheme here can be directly extended to hybrid [34,35] and multipartite [36] entanglement swapping. Our results pave the way for assembling all-optical quantum repeater and further constructing measurement-free all-optical broadband quantum network.

This work was funded by Innovation Program of Shanghai Municipal Education Commission (Grant No. 2021-01-07-00-08-E00100); the National Natural Science Foundation of China (11874155, 91436211, 11374104, 12174110); Basic Research Project of Shanghai Science and Technology Commission (20JC1416100); Natural Science Foundation of Shanghai (17ZR1442900); Minhang Leading Talents (201971); Shanghai Sailing Program (21YF1410800); Shanghai Municipal Science and Technology Major Project (2019SHZDZX01); the 111 project (B12024).

*Corresponding author.
jtjing@phy.ecnu.edu.cn

[1] Z.-S. Yuan, Y.-A. Chen, B. Zhao, S. Chen, J. Schmiedmayer, and J.-W. Pan, Nature (London) **454**, 1098 (2008).
[2] M. Żukowski, A. Zeilinger, M. A. Horne, and A. K. Ekert, Phys. Rev. Lett. **71**, 4287 (1993).
[3] S. L. Braunstein and P. van Loock, Rev. Mod. Phys. **77**, 513 (2005).
[4] C. Weedbrook, S. Pirandola, R. García-Patrón, N. J. Cerf, T. C. Ralph, J. H. Shapiro, and S. Lloyd, Rev. Mod. Phys. **84**, 621 (2012).
[5] J-W. Pan, D. Bouwmeester, H. Weinfurter, and A. Zeilinger, Phys. Rev. Lett. **80**, 3891 (1998).
[6] T. Jennewein, G. Weihs, J-W. Pan, and A. Zeilinger, Phys. Rev. Lett. **88**, 017903 (2001).
[7] X.-S. Ma, S. Zotter, J. Kofler, R. Ursin, T. Jennewein, Č. Brukner, and A. Zeilinger, Nat. Phys. **8**, 479 (2012).
[8] M. Halder, A. Beveratos, N. Gisin, V. Scarani, C. Simon, and H. Zbinden, Nat. Phys. **3**, 692 (2007).
[9] Y. Zhang, M. Agnew, T. Roger, F. S. Roux, T. Konrad, D. Faccio, J. Leach, and A. Forbes, Nat. Commun. **8**, 632 (2017).
[10] W. Ning, X. J. Huang, P. R. Han, H. Li, H. Deng, Z. B. Yang, Z. R. Zhong, Y. Xia, K. Xu, D. Zheng, and S. B. Zheng, Phys. Rev. Lett. **123**, 060502 (2019).
[11] R. E. S. Polkinghorne and T. C. Ralph, Phys. Rev. Lett. **83**, 2095 (1999).
[12] S. M. Tan, Phys. Rev. A **60**, 2752 (1999).
[13] P. van Loock and S. L. Braunstein, Phys. Rev. A **61**, 010302 (R) (1999).
[14] X. Jia, X. Su, Q. Pan, J. Gao, C. Xie, and K. Peng, Phys. Rev. Lett. **93**, 250503 (2004).
[15] N. Takei, H. Yonezawa, T. Aoki, and A. Furusawa, Phys. Rev. Lett. **94**, 220502 (2005).
[16] T. C. Ralph, Opt. Lett. **24**, 348 (1999).
[17] S. Liu, Y. Lou, and J. Jing, Nat. Commun. **11**, 3875 (2020).
[18] S. Takeda and A. Furusawa, APL Photonics **4**, 060902 (2019).
[19] C. F. McCormick, V. Boyer, E. Arimonda, and P. D. Lett, Opt. Lett. **32**, 178 (2007).
[20] V. Boyer, A. M. Marino, R. C. Pooser, and P. D. Lett, Science **321**, 544 (2008).
[21] A. M. Marino, R. C. Pooser, V. Boyer, and P. D. Lett, Nature **457**, 859 (2009).
[22] R. C. Pooser, A. M. Marino, V. Boyer, K. M. Jones, and P. D. Lett, Phys. Rev. Lett. **103**, 010501 (2009).
[23] S. Liu, Y. Lou, and J. Jing, Phys. Rev. Lett. **123**, 113602 (2019).
[24] A. Einstein, B. Podolsky, and N. Rosen, Phys. Rev. **47**, 777 (1935).

[25] M. Jasperse, L. D. Turner, and R. E. Scholten, Opt. Express **19**, 3765 (2011).
[26] L. M. Duan, G. Giedke, J. I. Cirac, and P. Zoller, Phys. Rev. Lett. **84**, 2722 (2000).
[27] R. Simon, Phys. Rev. Lett. **84**, 2726 (2000).
[28] See Supplemental Material at http://link.aps.org/supplemental/10.1103/PhysRevLett.128.060503 for the entanglement of the swapped pair, loss tolerance of the classical all-optical channel, the bandwidth of EPR entanglement, and the discrepancy between theory and experiment, which includes Ref. [29].
[29] C. F. McCormick, A. M. Marino, V. Boyer, and P. D. Lett, Phys. Rev. A **78**, 043816 (2008).
[30] F. A. S. Barbosa, A. S. Coelho, A. J. de Faria, K. N. Cassemiro, A. S. Villar, P. Nussenzveig, and M. Martinelli, Nat. Photonics **4**, 858 (2010).
[31] R. F. Werner and M. M. Wolf, Phys. Rev. Lett. **86**, 3658 (2001).
[32] A. S. Coelho, F. A. S. Barbosa, K. N. Cassemiro, A. S. Villar, M. Martinelli, and P. Nussenzveig, Science **326**, 823 (2009).
[33] N. Takanashi, A. Inoue, T. Kashiwazaki, T. Kazama, K. Enbutsu, R. Kasahara, T. Umeki, and A. Furusawa, Opt. Express **28**, 34916 (2020).
[34] S. Takeda, M. Fuwa, P. van Loock, and A. Furusawa, Phys. Rev. Lett. **114**, 100501 (2015).
[35] G. Guccione, T. Darras, H. Le Jeannic, V. B. Verma, S. W. Nam, A. Cavaillès, and J. Laurat, Sci. Adv. **6**, eaba4508 (2020).
[36] X. Su, C. Tian, X. Deng, Q. Li, C. Xie, and K. Peng, Phys. Rev. Lett. **117**, 240503 (2016).